

Modeling and Analysis of Piezoelectric Energy Harvesting From Aeroelastic Vibrations Using the Doublet-Lattice Method

Carlos De Marqui, Jr.¹
e-mail: demarqui@sc.usp.br

Wander G. R. Vieira
e-mail: wandergrv@gmail.com

Department of Aeronautical Engineering,
Engineering School of São Carlos,
University of São Paulo,
13566-590, São Carlos, São Paulo, Brazil

Alper Erturk
e-mail: erturk@vt.edu

Daniel J. Inman
e-mail: dinman@vt.edu

Department of Mechanical Engineering,
Center for Intelligent Material Systems and
Structures,
Virginia Polytechnic Institute and State
University, Blacksburg, VA 24061-0002

Multifunctional structures are pointed out as an important technology for the design of aircraft with volume, mass, and energy source limitations such as unmanned air vehicles (UAVs) and micro air vehicles (MAVs). In addition to its primary function of bearing aerodynamic loads, the wing/spar structure of an UAV or a MAV with embedded piezoceramics can provide an extra electrical energy source based on the concept of vibration energy harvesting to power small and wireless electronic components. Aeroelastic vibrations of a lifting surface can be converted into electricity using piezoelectric transduction. In this paper, frequency-domain piezoaeroelastic modeling and analysis of a cantilevered platelike wing with embedded piezoceramics is presented for energy harvesting. The electromechanical finite-element plate model is based on the thin-plate (Kirchhoff) assumptions while the unsteady aerodynamic model uses the doublet-lattice method. The electromechanical and aerodynamic models are combined to obtain the piezoaeroelastic equations, which are solved using a p-k scheme that accounts for the electromechanical coupling. The evolution of the aerodynamic damping and the frequency of each mode are obtained with changing airflow speed for a given electrical circuit. Expressions for piezoaeroelastically coupled frequency response functions (voltage, current, and electrical power as well the vibratory motion) are also defined by combining flow excitation with harmonic base excitation. Hence, piezoaeroelastic evolution can be investigated in frequency domain for different airflow speeds and electrical boundary conditions.

[DOI: 10.1115/1.4002785]

1 Introduction

An interesting trade-off exists between the increasing military demand for size and weight reduction of unmanned air vehicles (UAVs) and the total flight duration as required by a given mission. A major limitation for small UAVs is the energy required for long endurance missions [1]. The limitations in the available volume and the energy sources reduce the endurance and the flight range. Generating usable electrical energy during the mission of a UAV can relieve the auxiliary power drains or provide the power required for its sensors. Recently, researchers have investigated harvesting solar and vibration energy to provide an additional source of energy for UAVs [2–5].

The concept of energy harvesting has been pointed out as a future breakthrough technology for UAV design [6]. Wing structures must not only perform their primary function of load bearing but also be able to generate electricity. Researchers have added solar panels [2,3] over the wing skin of UAVs to power small electronic devices or to charge batteries for possible night flight missions. Another possible source of energy for UAVs is the mechanical vibration energy due to unsteady aerodynamic loads during the flight [2] or due to ground excitation in perching [3,5]. Although other transduction mechanisms exist, piezoelectric transduction has received the most attention for vibration-based energy harvesting due to the large power densities and ease of applications of piezoelectric materials as summarized in the existing review articles [7–10]. Recently, the concept of self-charging structures [11] has been introduced to improve multifunctionality

in UAVs. The proposed multilayer structure is composed of piezoceramic layers for vibration-to-electric energy conversion, thin-film battery layers for storing the generated energy, and a metallic substructure layer as the original load-bearing layer.

Literature of aeroelasticity includes research on using active controllers with piezoelectric elements and other types of smart materials as actuators to modify the aeroelastic behavior of wings [12–15]. The effect of passive controllers on the aeroelastic response of a structure has also been investigated by some authors [16–18]. The main goal of these papers is to increase overall damping of the aeroelastic system by employing piezoelectric materials with an external shunt circuit. However, the possibility of generating electrical power from airflow excitation has not been investigated in relevant literature.

Although most of literature covers harmonic excitation for vibration energy harvesting, analysis of energy harvesting from aeroelastic vibrations is more involved. Bryant and Garcia [19] presented a two degree of freedom typical section model as a piezoelectric power harvesting device driven by aeroelastic vibrations. The main motivation is to have an alternative energy source for placement in urban areas. A switching energy extracting scheme is used in order to increase the power extraction of the aeroelastic energy harvester. Recently, time-domain piezoaeroelastic modeling of a generator wing with embedded piezoceramics has been presented [4,20]. The model is obtained from the combination of an electromechanically coupled finite element (FE) model [21] with an unsteady vortex lattice method (VLM). The conversion of aeroelastic vibrations into electrical energy is investigated at several airflow speeds for a set of resistive loads. The aeroelastic behavior and the power generated are dependent on aerodynamic damping, which is modified with increasing airflow speed. At the flutter boundary (which depends on the external load resistance), the aerodynamic damping vanishes

¹Corresponding author.

Contributed by the Technical Committee on Vibration and Sound of ASME for publication in the JOURNAL OF VIBRATION AND ACOUSTICS. Manuscript received January 22, 2010; final manuscript received July 2, 2010; published online December 8, 2010. Assoc. Editor: Dane Quinn.

and the oscillations are persistent. Although this condition is usually avoided in a real aircraft, it is the simplest case for the concept demonstration of a generator wing using a linear piezoaeroelastic model. The response history with the largest instantaneous power output at the linear flutter speed shows a decaying behavior, which is due to the shunt damping effect of power generation. The effect of using segmented electrodes on the piezoaeroelastic response of the same generator wing and the same set of resistive loads has also been investigated [4]. The electrodes are segmented on the center line (midchord position) and properly combined to the electrical load to avoid the cancellation of the potential electrical output of the torsion-dominated modes. As a consequence of the improved electromechanical coupling, better power generation and shunt damping effects are obtained for the aeroelastic behavior since the piezoelectric reaction of the torsion mode in the coupled aeroelastic motions of flutter is taken into account with the segmented-electrode configuration. Although the time-domain linear piezoaeroelastic model can be used to simulate the piezoaeroelastic response at different airflow speeds, VLM is computationally expensive for repeated simulations (which are required to determine the optimum conditions in the energy harvesting circuit of the generator wing).

In this paper, frequency-domain piezoaeroelastic analysis of a generator wing with continuous electrodes is presented for energy harvesting. The piezoaeroelastic model is obtained by combining an unsteady aerodynamic model with an electromechanically coupled FE model [21]. The subsonic unsteady aerodynamic model is based on the doublet-lattice method (DLM) [22]. The piezoaeroelastic equations are solved using a p-k scheme [23] that accounts for the electrical domain of the problem. The evolution of overall damping for each mode with increasing airflow speed is obtained for a given electrical boundary condition. Piezoaeroelastically coupled frequency response functions (FRFs) (relative tip motion, voltage, current, and electrical power) are also used for a desired airflow speed and external circuit by combining the base excitation condition and the unsteady aerodynamic influence in the piezoaeroelastic equations. Two case studies are presented in this work. The first case considers a resistive load in the electrical domain. The piezoaeroelastic FRFs are presented for several airflow speed-load resistance combinations. The effect of aerodynamic damping and the resulting mode coupling with increasing airflow speed over the aeroelastic evolution of the generator wing are discussed along with its energy harvesting performance. A procedure is also presented in order to obtain the optimum load resistance (for the maximum power and the maximum damping) for a given airflow speed. After that, a resistive-inductive circuit (in series connection) is considered in the electrical domain. The optimum inductance is calculated for a target frequency (the short-circuit flutter frequency here) as presented in literature for the case of simple harmonic motion [24,25]. The resistor for the maximum power and damping is obtained using the same procedure of the first case study. The energy harvesting performance and the aeroelastic behavior are investigated and compared against the optimum condition of the resistive circuit case using the piezoaeroelastically coupled FRFs and the p-k solution.

2 Frequency Domain Piezoaeroelastic Model

The piezoaeroelastic model is obtained by combining an electromechanically coupled FE model with an unsteady doublet-lattice aerodynamic model. The electromechanically coupled FE model of the thin cantilevered wing with embedded piezoceramic layers shown in Fig. 1 is based on the Kirchhoff assumptions. The substructure and the piezoceramic layers are assumed to be perfectly bonded to each other. The piezoceramic layers (which are poled in the thickness direction) are covered by continuous electrodes (which are assumed to be perfectly conductive) with negligible thickness. A resistive load and a resistive-inductive circuit will be considered in the electrical domain. The purpose is to estimate the power generated in the electrical domain due to the

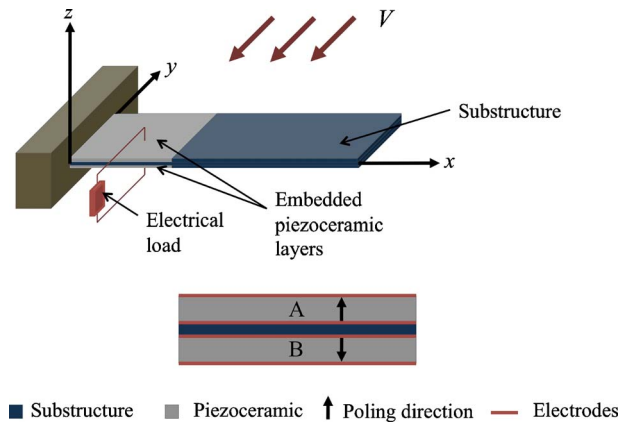


Fig. 1 Thin cantilevered wing with embedded piezoceramic layers and its cross-sectional view

aeroelastic vibrations of the energy harvester wing as well as the effect of electrical power generation on the aeroelastic behavior of the wing. A rectangular finite element with four nodes and three mechanical degrees of freedom per node is used to model the substructure. An electrical degree of freedom is added to the finite element to model the piezoceramic layers (13 degrees of freedom in total). A transformation is imposed in order to account for the presence of continuous and conductive electrodes bracketing each piezoceramic layer. Therefore a single electrical output is obtained from each piezoceramic layer. The reader is referred to Ref. [21] for the detailed derivation and validation of the electromechanically coupled FE model against the analytical and the experimental results.

The governing piezoaeroelastic equations for the generator wing (Fig. 1) are

$$\mathbf{M}\ddot{\Psi} + \mathbf{C}\dot{\Psi} + \mathbf{K}\Psi - \tilde{\Theta}v_p = \mathbf{F} \quad (1a)$$

$$\bar{C}_p \dot{v}_p + v_p Y + \tilde{\Theta}^T \Psi = 0 \quad (1b)$$

where \mathbf{M} is the global mass matrix, \mathbf{K} is the global stiffness matrix, \mathbf{C} is the global damping matrix (assumed to be proportional to the mass and the stiffness matrices), $\tilde{\Theta}$ is the effective electromechanical coupling vector, v_p is the resultant voltage output across the piezoceramics, \bar{C}_p is the effective capacitance of the piezoceramic, Y is the admittance of the external circuit, and Ψ is the global vector of mechanical coordinates. It is known from literature [26,27] that the electrode pairs covering each piezoceramic layer of a bimorph (Fig. 1) can be connected in series or in parallel to the external electrical load (for larger voltage or current). In general, the piezoceramic layers are poled in the same direction for parallel connection whereas they are poled in the opposite direction for series connection. For the parallel connection case, the effective electromechanical coupling vector is the sum of the individual contribution of each layer and the effective capacitance is the sum of each individual capacitances. For the series connection case, the effective electromechanical coupling vector is equal to that of one piezoceramic layer and the effective capacitance is one-half of the capacitance of one piezoceramic layer. In the case studies presented here, the continuous electrodes covering the piezoceramic layers (poled in the opposite directions) are connected in series to an external circuit. The right-hand-side term \mathbf{F} of the mechanical equation (Eq. (1a)) is the vector of unsteady aerodynamic loads obtained from the unsteady DLM.

2.1 The Doublet Lattice Model. The linearized formulation for the oscillatory, inviscid, subsonic lifting surface theory relates the normal velocity at the surface of a body (e.g., an elastic wing) with the aerodynamic loads caused by the pressure distribution

[22]. The formulation is derived using the unsteady Euler equations of the surrounding fluid. The doublet singularity (or a sheet of doublets) is a solution of the aerodynamic potential equation. An unsteady aeroelastic behavior as well as the resultant differential pressure across the surface of a wing can be represented with this solution.

The relation between the differential pressure across the surfaces and the velocity normal to the surface of a wing is given by a kernel function [22]. The kernel function is a closed-form solution of the integro-differential equation based on the assumption of harmonic motion. The velocity field normal to the surface of a wing is given by the equation

$$\bar{w}(x,y,z) = \frac{-1}{4V\pi\rho_o} \int \int_S \Delta p(x,y,z) K(x-\xi, y-\eta, z) d\xi d\eta \quad (2)$$

where $\Delta p(x,y,z)$ is the differential pressure, V is the freestream velocity, ρ_o is the density of the air, ξ and η , respectively, are dummy variables of integration over the area S of the wing in x (spanwise) and y (chordwise) direction, z is the transverse direction, and K is the kernel function. The kernel function is given as

$$K(x-\xi, y-\eta, z) = \exp\left(\frac{-j\omega(x-\xi)}{V}\right) \frac{\partial^2}{\partial z^2} \left[\frac{1}{\bar{R}} \exp\left[\frac{j\omega}{V\beta^2}(\lambda - M\bar{R})\right] d\lambda \right] \quad (3)$$

where $\beta^2 = 1 - M^2$ and $\bar{R} = \sqrt{(x-\xi)^2 + (y-\eta)^2 + z^2}$, ω is the frequency of excitation, M is the Mach number, and λ is a dummy variable.

DLM provides a numerical approximation for the solution of the kernel function. The wing is represented by a thin lifting surface and it is divided into a number of elements (panels or boxes) with doublet singularities of constant strength in chordwise and parabolic strength in spanwise direction. A line of doublets (distribution of acceleration potential) is assumed at the 1/4 chord line of each panel, which is equivalent to a pressure jump across the surface. A control point is defined in the half span of each box at the 3/4 chord line (the point where the boundary condition is verified). The strength of the oscillating potential placed at the 1/4 chord lines are the unknowns of the problem.

The prescribed downwash (as the solution is assumed to be harmonic) introduced by the lifting lines is checked at each control point. The solution of the resulting matrix equation is

$$\frac{\bar{w}}{V} = \mathbf{A}\Delta\mathbf{C}_p \quad (4)$$

which gives the strength of the lifting line at each panel and consequently, the pressure distribution across the surface. Here, \mathbf{A} is the matrix of influence (which is related to kernel function) between the normal velocity and the nondimensional pressure distribution $\Delta\mathbf{C}_p$. Integration over the surface gives the local and the total aerodynamic force coefficients [22].

2.2 Piezoaerostically Coupled Equations of Motion. The aerodynamic loads can be included in the piezoaerostatic equations as an aerodynamic matrix of influence coefficients. The aerodynamic loads and the structural motion are obtained from distinct numerical methods with distinct meshes. Therefore, the transformation matrices are determined using a surface spline scheme in order to interpolate the forces obtained in the doublet-lattice mesh to the nodes of the FE mesh [28]. The resulting

Table 1 Admittances for different external circuits

External circuit	Resistive	Resistive-inductive (in series)	Resistive-inductive (in parallel)
Admittance	$\frac{1}{R_I}$	$\frac{1}{R_I + j\omega L}$	$\frac{1}{R_I} + \frac{1}{j\omega L}$

displacements of the structural mesh are also interpolated at the corners of the aerodynamic mesh.

Since the unsteady aerodynamic solution is assumed to be harmonic, the piezoaerostatic equations (Eqs. (1a) and (1b)) in modal domain can be presented as

$$(-\omega^2\bar{\mathbf{M}} + j\omega\bar{\mathbf{C}} + \bar{\mathbf{K}} - q\mathbf{Q})\boldsymbol{\eta} - \Phi'\tilde{\Theta}v_p = 0 \quad (5a)$$

$$C_p j\omega v_p + v_p Y(\omega) + j\omega\tilde{\Theta}'\Phi\boldsymbol{\eta} = 0 \quad (5b)$$

where the overbars represent modal matrices, $\boldsymbol{\eta}$ is the vector of modal displacements, Φ is the modal matrix, and q is the dynamic pressure, \mathbf{Q} is the aerodynamic influence matrix, j is the unit imaginary number, and ω is the excitation frequency. The admittance $Y(\omega)$ depends on the external circuit. The admittance expressions for the resistive and the resistive-inductive (in series and in parallel) circuits are presented in Table 1.

The conventional p-k scheme is one of the available ways to address the flutter equations for unsteady aerodynamic theories with the harmonic motion assumption [29]. In this method, the evolution of the frequencies and damping is iteratively investigated for different airflow speeds (or reduced frequencies), solving the following eigenvalue problem for a conventional wing

$$p \begin{Bmatrix} \mathbf{h}_1 \\ \mathbf{h}_2 \end{Bmatrix} = \begin{bmatrix} 0 & \mathbf{I} \\ -\bar{\mathbf{M}}^{-1}(\bar{\mathbf{K}} - q\mathbf{Q}^R) & -\bar{\mathbf{M}}^{-1}(\bar{\mathbf{C}} - q\mathbf{Q}^I) \end{bmatrix} \begin{Bmatrix} \mathbf{h}_1 \\ \mathbf{h}_2 \end{Bmatrix} \quad (6)$$

where $\mathbf{h}_1 = \boldsymbol{\eta}$ and $\mathbf{h}_2 = p\boldsymbol{\eta}$, the superscripts R and I stand for the real and the imaginary parts of the aerodynamic matrix, p is the eigenvalue of the problem, which gives the frequency (related to the imaginary part) and damping (related to the real part). However, Eqs. (5a) and (5b) differ from the conventional aeroelastic equations due to the presence of piezoelectric layers and an external generator circuit (electromechanical coupling in the mechanical equation and the electrical equation, Eqs. (5a) and (5b)). Therefore, the conventional p-k scheme is modified to solve the piezoaerostatic problem for different electrical boundary conditions. For the first case (a resistive load), an augmented system is solved to examine the piezoaerostatic behavior with increasing airflow speed and one specific load resistance using

$$p \begin{Bmatrix} \mathbf{h}_1 \\ \mathbf{h}_2 \\ h_3 \end{Bmatrix} = \begin{bmatrix} \mathbf{0} & \mathbf{I} & \mathbf{0} \\ -\bar{\mathbf{M}}^{-1}(\bar{\mathbf{K}} - q\mathbf{Q}^R) & -\bar{\mathbf{M}}^{-1}(\bar{\mathbf{C}} - q\mathbf{Q}^I) & \bar{\mathbf{M}}^{-1}(\Phi'\tilde{\Theta}) \\ \mathbf{0} & -\frac{\tilde{\Theta}'\Phi}{C_p} & -\frac{1}{C_p R_I} \end{bmatrix} \begin{Bmatrix} \mathbf{h}_1 \\ \mathbf{h}_2 \\ h_3 \end{Bmatrix} \quad (7)$$

where $\mathbf{h}_1 = \boldsymbol{\eta}$, $\mathbf{h}_2 = p\boldsymbol{\eta}$, and $h_3 = v_p$. The solution still gives the evolution of frequency and damping of the modes with increasing airflow speed, but here, the electromechanical coupling and the effect of a load resistance connected to the piezoceramic layer are included. When a resistive-inductive circuit (in series) is considered in the electrical domain of this piezoaerostatically problem, the new augmented system becomes

$$P \begin{Bmatrix} \mathbf{h}_1 \\ \mathbf{h}_2 \\ h_3 \\ h_4 \end{Bmatrix} = \begin{bmatrix} \mathbf{0} & \mathbf{I} & \mathbf{0} & \mathbf{0} \\ -\bar{\mathbf{M}}^{-1}(\bar{\mathbf{K}} - q\mathbf{Q}^R) & -\bar{\mathbf{M}}^{-1}(\bar{\mathbf{C}} - q\mathbf{Q}^I) & \bar{\mathbf{M}}^{-1}(\Phi' \tilde{\Theta}) & \mathbf{0} \\ \mathbf{0} & \mathbf{0} & \mathbf{0} & \mathbf{I} \\ -\bar{\mathbf{M}}^{-1} \frac{\Phi \tilde{\Theta}' (\bar{\mathbf{K}} - q\mathbf{Q}^R)}{C_p} & -\bar{\mathbf{M}}^{-1} \frac{\Phi \tilde{\Theta}' (\bar{\mathbf{C}} - q\mathbf{Q}^I)}{C_p} - \frac{\Phi \tilde{\Theta}' R_l}{C_p L} & -\bar{\mathbf{M}}^{-1} \frac{\Phi \tilde{\Theta}' \Phi' \tilde{\Theta}}{C_p} - \frac{1}{C_p L} & -\frac{R_l}{L} \end{bmatrix} \begin{Bmatrix} \mathbf{h}_1 \\ \mathbf{h}_2 \\ h_3 \\ h_4 \end{Bmatrix} \quad (8)$$

where $\mathbf{h}_1 = \boldsymbol{\eta}$, $\mathbf{h}_2 = p\boldsymbol{\eta}$, $h_3 = v_p$ (voltage output), and $h_4 = pv_p$. This solution gives the aeroelastic evolution of the modes with increasing airflow speed considering the effect of a resonant circuit. Although the main motivation here is electrical power generation, this formulation can be used to investigate the influence of the electrical domain (a resistive, resistive-inductive, or a more complex circuit) on the aeroelastic behavior of a generator wing.

2.3 Piezoaeroelastically Coupled FRFs. In addition to the p-k scheme (which gives the neutral stability limit), the piezoaeroelastic behavior can be investigated in terms of piezoaeroelastically coupled FRFs. The FRFs are defined using Eqs. (5a) and (5b) by assuming an imposed base excitation condition in the piezoaeroelastic problem. Therefore, the forcing term in Eq. (1a) is modified as

$$\mathbf{F} = \mathbf{F}_{\text{aero}} + \mathbf{F}_b \quad (9)$$

where \mathbf{F}_{aero} is the unsteady aerodynamic loads determined using the DLM ($\mathbf{F}_{\text{aero}} = q\mathbf{Q}$) and \mathbf{F}_b is due to the base excitation. As discussed in literature [30], if the base is vibrating in the transverse direction (z -direction), the effective force on the structure is due to the inertia of the structure acting on the structure in the opposite direction. Therefore, the forcing term \mathbf{F}_b is represented as

$$\mathbf{F}_b = -\mathbf{m}^* a_b \quad (10)$$

where \mathbf{m}^* is the vector of effective mass per unit area obtained from the FE solution (including both the piezoceramic and/or the substructure layers) and a_b is the base acceleration. Assuming harmonic motion with the influence of the unsteady aerodynamics, the piezoaeroelastically coupled FRFs are defined by the matrix equation

$$\boldsymbol{\alpha} = \begin{bmatrix} -\omega^2 \bar{\mathbf{M}} + j\omega \bar{\mathbf{B}} + \bar{\mathbf{K}} - q\mathbf{Q} & -\Phi' \tilde{\Theta} \\ j\tilde{\Theta}' \Phi \omega & jC_p \omega + Y(\omega) \end{bmatrix} \mathbf{m}^* \quad (11)$$

where $\boldsymbol{\alpha}$ is an $(n+1) \times 1$ vector containing the n modal displacements per base acceleration (n is the number of modes considered in the solution) for a desired airflow speed. The $(n+1)$ th line gives the steady-state voltage FRF defined here as the voltage across the load per base acceleration for a desired airflow speed. In addition to the voltage FRF, one might as well define the power FRF. Assuming a resistive or a resistive-inductive circuit in parallel connection, one can obtain the electric current FRF by dividing the voltage FRF by the load resistance R_l of the energy harvesting circuit. The electrical power FRF is the product of the voltage and current FRFs and it is defined as the ratio of electrical power output to the square of the base acceleration. When a resistive-inductive in series external circuit is used, it is important to note that the voltage across the electrodes of the piezoceramic layer and the voltage across the load resistance are different. Therefore, the voltage across the load resistance has to be calculated to define the electrical power FRF properly.

When a simple resistive load is considered in the electrical circuit, the variation of power output with load resistance at the short-circuit resonance frequency of a specific mode for a desired airflow speed can be investigated. Also, the optimum load resistance for the maximum power or the maximum shunt damping can be determined for a desired airflow speed and vibration mode

of interest. The typical aeroelastic behavior at the speed of neutral stability condition results in continuous power generation, i.e., the modes are coupled at the flutter frequency, and self-sustained oscillations are obtained. The optimum load resistance can be determined at the flutter speed (or at airflow speeds slightly lower than the flutter speed) by exciting the generator wing at the short-circuit flutter frequency and investigating the power output. The optimum load resistance for the maximum resistive shunt damping effect can also be determined by exciting the generator wing at the short-circuit flutter frequency and investigating the relative tip motion. A similar procedure can also be employed when resistive-inductive external circuits are used. First, the inductance requirement for a specific target frequency is obtained. One can then search for the optimum resistance for best power or shunt damping effect following the procedure described previously.

3 Results

This section investigates the piezoaeroelastic behavior of a cantilevered platelike wing with embedded piezoceramics for two different external circuits. First, a resistive load is considered in the electrical domain. Damping and frequency evolution of the vibration modes are obtained with increasing airflow speed at the short-circuit condition (assuming $R_l = 100 \Omega$ to be close to short-circuit) using the p-k scheme described herein to obtain the linear flutter speed and frequency. The electromechanical behavior of the generator wing is then presented by using the piezoaeroelastically coupled FRFs close to the short-circuit condition for several airflow speeds (from low airflow speeds to the linear flutter speed). The optimum load resistance for the maximum power generation and the maximum shunt damping effect at the flutter speed are also determined. Using the optimum load resistance that gives the maximum power output, the piezoaeroelastically coupled FRFs are compared with those close to the short-circuit conditions. Later, a resistive-inductive load (series connection) is used in the electrical domain. The optimal inductor-resistor pair is determined for the maximum power output. Damping and frequency evolution of the vibration modes are investigated with increasing airflow speed and a modified flutter speed is obtained. Also, the piezoaeroelastically coupled FRFs for the resistive-inductive case are compared against the resistive case at the flutter speed. The effect of resistive-inductive shunting on the flutter boundary is also investigated.

Two identical layers of PZT-5A are embedded into the top and the bottom of the plate at the root. Conductive electrodes covering the upper and the lower faces of the piezoceramic layers are connected in series to a resistive electrical load as depicted in Fig. 1. The dimensions of the platelike wing considered in this work are $1200 \times 240 \times 3 \text{ mm}^3$. The identical piezoceramic layers have the same width as the wing chord. The embedded piezoceramic layers cover 30% of the wing span (from the root to the tip) and each one has a thickness of 0.5 mm. The geometric and the material properties of the wing (aircraft aluminum alloy Al 2024-T3) are presented in Table 2. Note that the length-to-thickness ratio of the wing is large enough to neglect the shear deformation and the rotary inertia effects for the vibration modes of interest. The proportionality constants shown in Table 2 give the modal mechanical damping ratios of the first three vibration modes (in the absence of airflow) as 0.01, 0.015, and 0.022, respectively. The

Table 2 Geometric and material properties of the aluminum wing with embedded piezoceramics

Length of the wing (mm)	1200
Width of the wing (mm)	240
Thickness of the wing (mm)	3
Young's modulus of the wing (GPa)	70.0
Mass density of the substructure (kg/m ³)	2750
Proportional constant: α (rad/s)	0.1635
Proportional constant: β (s/rad)	4.1711×10^{-4}

typical properties of PZT-5A piezoceramics are given in Table 3 [31] where $\epsilon_0=8.854$ pF/m is the permittivity of free space.

The mode sequence and the undamped natural frequencies of the platelike wing obtained from the FE model close to short-circuit conditions ($R_f \rightarrow 0$) are presented in Table 4. The first five modes are listed where B and T stand for the bending and the torsion modes, respectively. It is important to note that the spanwise elastic axis and the center of gravity are coincident at 50% of the chord.

3.1 Piezoaeroelastic Analysis With a Resistive Electrical Circuit. The aeroelastic behavior of the generator wing close to short-circuit conditions ($R_f=100 \Omega$) is presented in terms of damping and frequency with increasing airflow speed in Figs. 2(a) and 2(b). The evolution of damping with airflow speed (Fig. 2(a)) shows the flutter instability for the short-circuit condition at 40 m/s. The frequency evolution and the coalescence of modes 2 (2B) and 3 (1T) with increasing airflow speed are observed in Fig. 2(b). Modes 1 (1B) and 5 (2T) are not shown in Figs. 2(a) and 2(b) for clarity.

The mode shape at the flutter condition is shown in Fig. 3. One can observe that, at the flutter speed, this is a coupled bending-torsion mode (second bending and first torsion). This mode shape agrees with the coalescence of the second bending and the first torsion modes observed at 40 m/s in Fig. 2(b).

The relative tip motion FRF and the electrical power output FRF are presented for several airflow speeds (from the no flow condition ($V=0$ m/s) to the flutter speed) in Figs. 4(a) and 4(b). The mechanical FRF is measured at the leading edge (LE) of the tip of the generator wing. The peaks of the first bending and the second bending modes are observed for zero airflow speed. Since the forcing term in the base excitation problem is related to the inertia of the structure in the direction of base motion [30], for

Table 3 Material and electromechanical properties of PZT-5A

Mass density (kg/m ³)	7800
Permittivity (nF/m)	$1800 \times \epsilon_0$
c_{11}^E, c_{22}^E (GPa)	120.3
c_{12}^E (GPa)	75.2
c_{13}^E, c_{23}^E (GPa)	75.1
c_{33}^E (GPa)	110.9
c_{66}^E (GPa)	22.7
e_{31}, e_{32} (C/m ²)	-5.2
e_{33} (C/m ²)	15.9

Table 4 Undamped natural frequencies and mode shapes

Mode	Mode shape	ω_{sc} (Hz)
1	1B	1.68
2	2B	10.46
3	1T	16.66
4	3B	27.74
5	2T	48.65

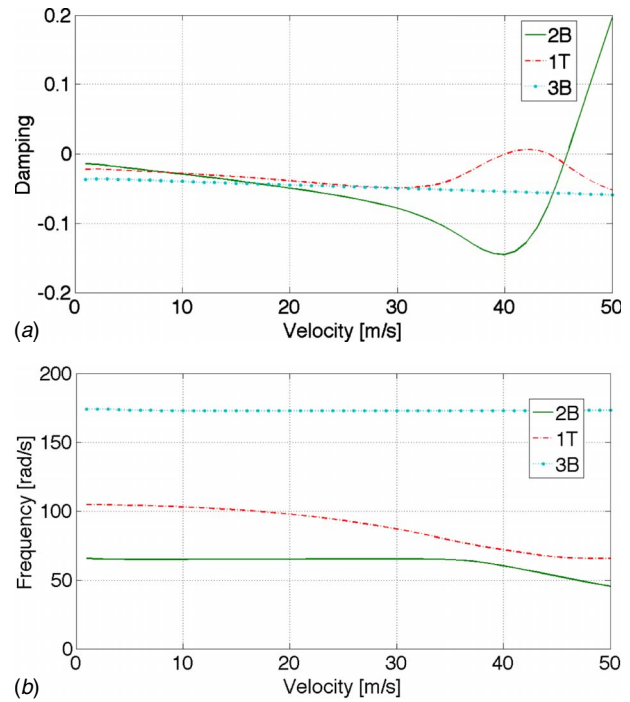


Fig. 2 (a) Damping evolution with increasing airflow speed and (b) frequency evolution with increasing airflow speed for the resistive circuit case close to short-circuit conditions ($R_f=100 \Omega$)

symmetric structures with respect to the center line (as the generator wing with symmetric mass distribution used here), one cannot observe the peaks related to pure torsional modes in the electromechanical FRFs for the base excitation condition without unsteady aerodynamic influence (i.e., for $V=0$ m/s). For instance, the resonance frequency of the first torsional mode is 16.6 Hz and no peak is observed for this frequency in Figs. 4(a) and 4(b) when $V=0$ m/s (torsion modes are not excited). The behavior is modified when the airflow speed is not zero (base excitation and unsteady aerodynamic influence). In typical aeroelastic response, bending and torsion modes are coupled with increasing airflow speed. Therefore, a peak is observed around 16 Hz for the airflow speed of 20 m/s in Fig. 4(a). However, this peak is not observed in the power FRF (Fig. 4(b)). At this airflow speed, the mode is a coupled bending-torsion mode dominated by torsional motion. The electrical output from torsional vibrations is canceled when continuous electrodes cover the piezoceramic layers of the generator wing [4]. At the airflow speed of 35 m/s, this peak is shifted to 13 Hz and still represents a bending-torsion mode. However, the response at this airflow speed is dominated by bending motion. As a result, one can observe a peak at this frequency in the power FRF of Fig. 4(b) (no complete cancellation). At the flutter speed (40 m/s), aerodynamic damping is zero and modes are coupled at the flutter frequency (11.47 Hz) and maximum tip displacement and power output are achieved. Power could be optimized if segmented electrodes were used (along with shorter piezoceramics due to the strain node of the second bending mode [32]) to avoid the cancellation of electrical outputs from the torsional component of the coupled bending-torsion motions of flutter. The effect of increasing airflow speed on the damping can also be observed in Figs. 4(a) and 4(b). Aerodynamic damping increases from 5 m/s to 35 m/s considerably due to the unsteady aerodynamic effects. The maximum aerodynamic damping is observed at an airflow speed of 35 m/s and this is not a favorable condition for power harvesting.

The optimum load resistance for the maximum power output at the flutter speed is determined next. The cantilevered end of the

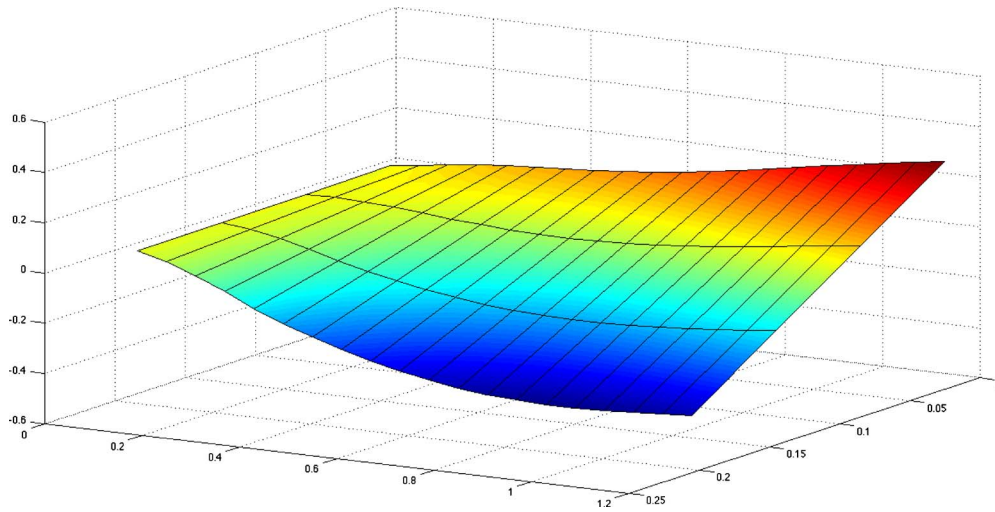


Fig. 3 Mode shape at the flutter speed (coupled bending-torsion mode)

generator wing is excited at the short-circuit flutter frequency (determined in Fig. 4, which is given for a load close to short-circuit conditions) and the maximum power output is obtained for a certain load resistance. The variation of the power output with load resistance at the short-circuit flutter frequency (11.47 Hz) for air-flow speed of 40 m/s is presented in Fig. 5. The maximum power output is obtained for $R_l = 15.8 \text{ k}\Omega$ as $4.6 \text{ mW s}^4/\text{m}^2$.

The electrical power output and the relative tip motion FRFs at the flutter speed are presented in Figs. 6(a) and 6(b), respectively, for two particular values of load resistance. The first load resistance is $R_l = 100 \text{ }\Omega$ (close to short-circuit conditions) and the second one is the optimum load resistance for the maximum power. Power amplitude is larger for the optimum load resistance over

the entire frequency range considered. As in the case of simple harmonic excitation [21,30], the resonance frequency depends on the load resistance. The shunt damping effect of resistive power dissipation is observed in the relative tip motion FRF. Although damping is introduced into the system and the amplitude of motion at the wing tip is reduced, the flutter speed is not significantly increased. The flutter speed for the optimum load resistance is 40.5 m/s (an increase of 0.5 m/s compared with the short-circuit flutter speed).

3.2 Piezoaeroelastic Analysis With a Resistive-Inductive Electrical Circuit. The piezoaeroelastic behavior of the wing is also investigated for the case when a resistor and an inductor are connected in series in the electrical domain. Increased power output and increased flutter speed (due to increased shunt damping effect of the resonant circuit) are expected by adjusting the inductor to the target frequency [24] (short-circuit flutter frequency) and searching for the optimum load resistance that gives the maximum power. Therefore, the piezoaeroelastically coupled FRFs for the series connection resistive-inductive case are compared against the FRFs obtained in the previous case study for the optimum load resistance ($R_l = 15.8 \text{ k}\Omega$) at the short-circuit flutter speed (40 m/s).

The flutter frequency of 11.47 Hz (determined close to the short-circuit condition of the resistive case) is taken as the target frequency to calculate the inductance of the series connection resistive-inductive generator circuit. The required inductance for the flutter frequency is calculated as 194 H [24,25]. Usually, synthetic inductance or impedance circuits [33,34] are employed to

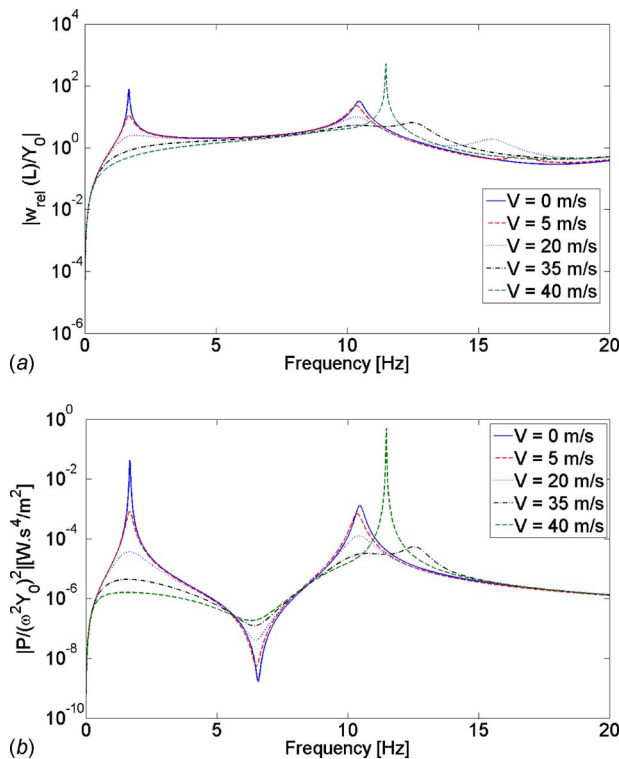


Fig. 4 (a) Relative tip motion FRFs and (b) power FRFs for various air flow speeds close to short-circuit conditions ($R_l = 100 \text{ }\Omega$)

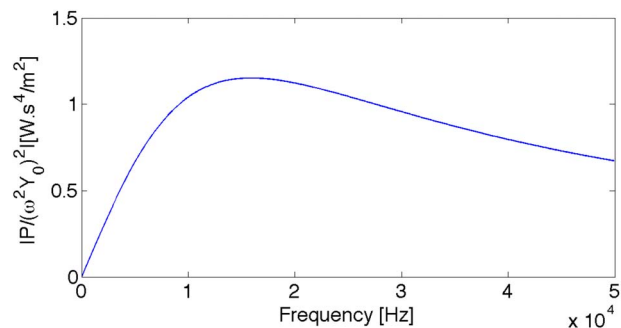


Fig. 5 Variation of electrical power output with load resistance at the short-circuit flutter speed and frequency for the resistive circuit case

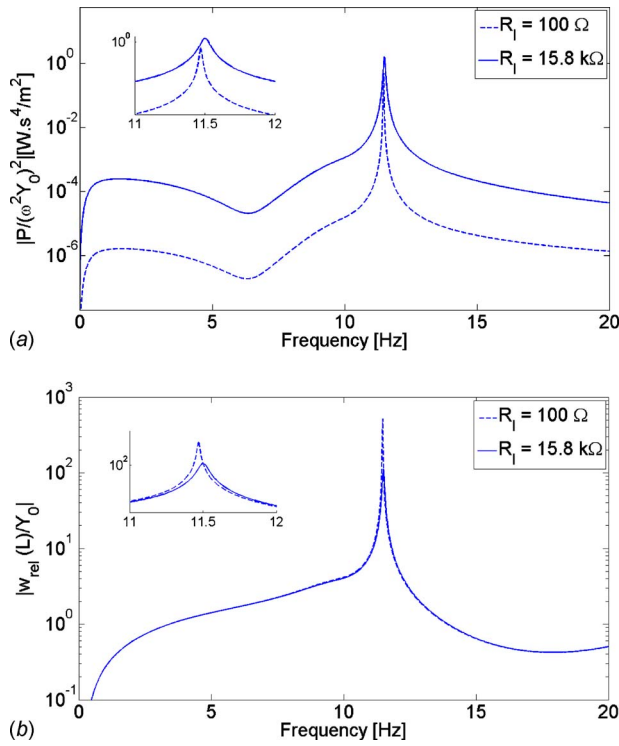


Fig. 6 (a) Power FRF and (b) relative tip motion FRF with close-up views around the flutter frequency at the short-circuit flutter speed for a load close to short-circuit conditions and for the optimum load resistance that gives the maximum power output

realize such large values of inductance. The optimum load resistance for the maximum power output at the short-circuit flutter speed is determined next. The cantilevered end of the generator wing is excited at the short-circuit flutter frequency (determined in Fig. 4, which is given for a load close to short-circuit conditions) and the maximum power output is obtained for a certain load resistance. The variation of the power output with load resistance at the short-circuit flutter frequency (11.47 Hz) for the airflow speed of 40 m/s and an inductance of 194 H is presented in Fig. 7. The maximum power output is observed for $R_l = 180 \Omega$.

The electrical power output and relative tip motion FRFs are presented in Figs. 8(a) and 8(b). The power output of the resistive-inductive case is larger than the power output of the resistive case in the range of frequencies considered here (except for frequencies lower than 2 Hz). Close to the short-circuit flutter frequency, the power generated from aeroelastic vibrations in the resistive-inductive configuration is about 20 times larger than the power

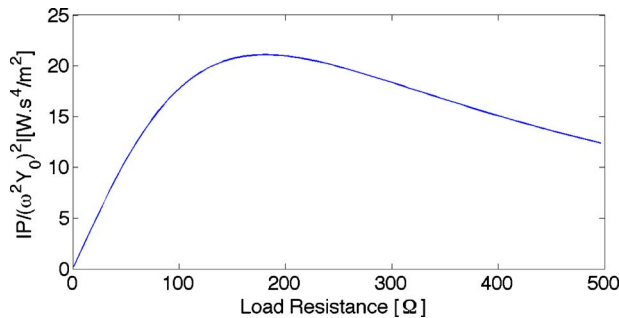


Fig. 7 Variation of electrical power output with load resistance at the short-circuit flutter speed and frequency for the resistive-inductive circuit case

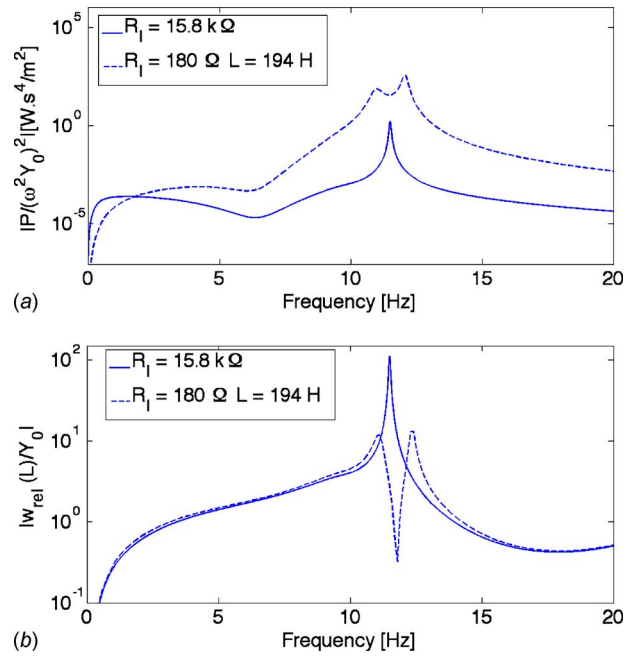


Fig. 8 (a) Power FRFs and (b) relative tip motion FRF at the short-circuit flutter speed for the optimum load resistance

generated when only a load resistance is considered in the electrical domain. The effect of power generation with the resistive-inductive circuit on the relative tip motion FRF (Fig. 8(b)) is observed around the short-circuit flutter frequency. It is important to recall that the optimum resistor for maximum power is $R_l = 180 \Omega$ (close to short-circuit conditions). Therefore, the flutter peak is split into two new peaks and an antiresonance appears close to the short-circuit flutter frequency in the mechanical FRF (also observed in power FRF). These peaks and the antiresonance would be damped (creating a plateau shaped displacement around the target frequency) if the optimum resistor for maximum damping is used [24,25]. Comparing Figs. 2(a) and 9(a), one can

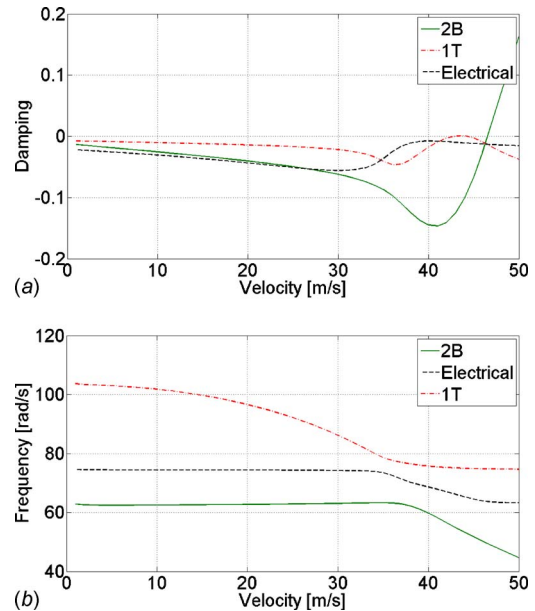


Fig. 9 (a) Damping evolution with increasing airflow speed and (b) frequency evolution with increasing airflow speed in the resistive-inductive case for the maximum damping

observe that the flutter speed is increased when the resistive-inductive circuit is used instead of the resistive one. Therefore, increased electrical power output of the resistive-inductive case comes with increased flutter speed.

Damping and frequency evolution of the modes of interest with increasing airflow speed for the maximum power is displayed in Figs. 9(a) and 9(b). It is important to note that a new mode appears when a resonant circuit is used in the electrical domain. This mode can be identified as the electrical mode by comparing the frequencies for low airflow speeds in Fig. 9(b) with the natural frequencies of the mechanical modes presented in Table 4 and with the frequencies for low airflow speeds of Fig. 2(b). Although the resistive-inductive shunt damping effect is reduced for this case (the resistance is obtained for maximum power), the flutter speed is 7.5% larger than the short-circuit flutter speed. It is important to recall that the main motivation here is power generation. If it is aimed to create the maximum damping effect, a different value for the load resistance is obtained [24]. Although not shown here, this configuration was tested ($R_l=2.2 \text{ k}\Omega$) and a flutter speed that is 15% larger than the short-circuit flutter speed is obtained due to the stronger resistive-inductive shunt damping effect.

4 Summary and Conclusions

The frequency-domain piezoaeroelastic model presented here has the important advantage of reducing the computational cost when compared with the time-domain piezoaeroelastic solution previously presented by the authors. The effect of piezoelectric power generation over the aeroelastic boundary of the wing is clearly observed with the p-k solution. A practical procedure is provided to search for the optimum components of the external circuit for maximum power output (or for maximum shunt damping) using the unsteady aerodynamics along with an imposed harmonic base excitation at a desired airflow speed. Piezoaeroelastically coupled FRFs are also defined with the combination of unsteady flow effects and harmonic base excitation. The magnitude of the electrical outputs (voltage, current, or power), the magnitude of mechanical variables, and the aeroelastic evolution can be investigated with the FRFs defined here at different airflow speeds and electrical conditions.

Two different external circuits, resistive and resistive-inductive in series, are considered in the electrical domain. For the case of a resistive load, the effects of the aerodynamic damping over the resonance frequencies and the modes coupling with increasing airflow speed are also clearly observed in the FRFs. The cancellation of the electrical output from torsion-dominated modes for the continuous-electrode case is observed by comparing the mechanical FRF (relative tip motion) with the power output FRF. The peak relative to a torsion-dominated coupled mode is observed around 16 Hz in the mechanical FRF after a certain airflow speed (20 m/s). However, this peak is not observed in the electrical FRF for the same speed since continuous electrodes are used in this work. The coupling is modified with increasing airflow speed. At 35 m/s, the coupled mode oscillates around 13 Hz. This is a bending-torsion mode dominated by bending motion. Therefore, with this airflow speed, an electrical output is observed for base excitation at this frequency. As a consequence, at the flutter speed and flutter frequency (where bending-torsion motion is observed), the cancellation of the out of phase electrical output occurs. The use of segmented electrodes could avoid the cancellation and improve the piezoaeroelastic behavior.

The performance of the piezoaeroelastically coupled wing is improved when a resistive-inductive circuit is used in the electrical domain. The power output is larger than the power obtained in the resistive case with the optimum load resistance over almost the entire range of frequencies investigated here. At the short-circuit flutter speed and short-circuit flutter frequency, power output is about 20 times larger than the resistive case. In addition to

the improved power generation a new flutter speed that is 7.5% larger than the short-circuit flutter speed of the resistive-inductive case is obtained.

Acknowledgment

The authors gratefully acknowledge the support of the Air Force Office of Scientific Research MURI under Grant No. F 9550-09-1-0625 "Simultaneous Vibration Suppression and Energy Harvesting" monitored by Dr. B. L. Lee. The authors also gratefully acknowledge CNPq and FAPEMIG for partially funding the present research work through the INCT-EIE.

References

- [1] Langelaan, J. W., 2007, "Long Distance/Duration Trajectory Optimization for Small UAVs," AIAA Guidance, Navigation and Control Conference and Exhibit, Hilton Head, SC.
- [2] Anton, S. R., and Inman, D. J., 2008, "Vibration Energy Harvesting for Unmanned Air Vehicles," *Proc. SPIE*, **6928**, p. 692824.
- [3] Magoteaux, K. C., Sanders, B., and Sodano, H. A., 2008, "Investigation of Energy Harvesting Small Unmanned Air Vehicle," *Proc. SPIE*, **6928**, p. 692823.
- [4] De Marqui, C., Jr., Erturk, A., and Inman, D. J., 2010, "Piezoaeroelastic Modeling and Analysis of a Generator Wing With Continuous and Segmented Electrodes," *J. Intell. Mater. Syst. Struct.*, **21**, pp. 983–993.
- [5] Erturk, A., Renno, J. M., and Inman, D. J., 2009, "Modeling of Piezoelectric Energy Harvesting From an L-Shaped Beam-Mass Structure With an Application to UAVs," *J. Intell. Mater. Syst. Struct.*, **20**, pp. 529–544.
- [6] Pines, D. J., and Bohorquez, F., 2006, "Challenges Facing Future Micro-Air-Vehicle Development," *J. Aircr.*, **43**, pp. 290–305.
- [7] Sodano, H. A., Inman, D. J., and Park, G., 2004, "A Review of Power Harvesting From Vibration Using Piezoelectric Materials," *The Shock and Vibration Digest*, **36**, pp. 197–205.
- [8] Priya, S., 2007, "Advances in Energy Harvesting Using Low Profile Piezoelectric Transducers," *J. Electroceram.*, **19**, pp. 167–184.
- [9] Anton, S. R., and Sodano, H. A., 2007, "A Review of Power Harvesting Using Piezoelectric Materials 2003–2006," *Smart Mater. Struct.*, **16**, pp. R1–R21.
- [10] Cook-Chennault, K. A., Thambi, N., and Sastry, A. M., 2008, "Powering MEMS Portable Devices—A Review of Non-Regenerative and Regenerative Power Supply Systems With Emphasis on Piezoelectric Energy Harvesting Systems," *Smart Mater. Struct.*, **17**, p. 043001.
- [11] Anton, S. R., Erturk, A., Kong, N., Ha, D. S., and Inman, D. J., 2009, "Self-Charging Structures Using Piezoceramics and Thin-Film Batteries," *Proceedings of the ASME Conference on Smart Materials, Adaptive Structures and Intelligent Systems*, Oxnard, CA.
- [12] Giurgiutiu, V., 2000, "Review of Smart-Materials Actuation Solutions for Aeroelastic and Vibration Control," *J. Intell. Mater. Syst. Struct.*, **11**, pp. 525–544.
- [13] Lazarus, K. B., Crawley, E. F., and Lin, C. Y., 1997, "Multivariable Active Lifting Surface Control Using Strain Actuation: Analytical and Experimental Results," *J. Aircr.*, **34**(3), pp. 313–321.
- [14] Lin, C. Y., Crawley, E. F., and Heer, J., 1996, "Open- and Closed-Loop Results of a Strain-Actuated Active Aeroelastic Wing," *J. Aircr.*, **33**(5), pp. 987–994.
- [15] Lazarus, K. B., Crawley, E. F., and Lin, C. Y., 1996, "Multivariable High-Authority Control of Plate-Like Active Structures," *J. Guid. Control Dyn.*, **19**(6), pp. 1357–1363.
- [16] Agneni, A., Mastroddi, F., and Polli, G. M., 2003, "Shunted Piezoelectric Patches in Elastic and Aeroelastic Vibrations," *Comput. Struct.*, **81**, pp. 91–105.
- [17] Agneni, A., Del Sorbo, M., Mastroddi, F., and Polli, G. M., 2006, "Multi-Modal Damping by Shunted Piezo-Patches: Possible Aeroelastic Applications," *Int. J. Appl. Electromagn. Mech.*, **24**, pp. 1–24.
- [18] McGowan, A. R., Heeg, J., and Lake, R., 1996, "Results of Wind-Tunnel Testing From the Piezoelectric Aeroelastic Tailoring Investigation," 37th AIAA/ASCE/AHS/ASC Structures, Structural Dynamics and Materials Conference.
- [19] Bryant, M., and Garcia, E., 2009, "Development of an Aeroelastic Vibration Power Harvester," *Proceedings of the Active and Passive Smart Structures and Integrated Systems 2009*.
- [20] De Marqui, C., Jr., Erturk, A., and Inman, D. J., 2009, "Piezoaeroelastically Coupled Modeling and Analysis of Electrical Power Generation and Shunt Damping for a Cantilever Plate," *Proceedings of the 17th International Conference on Composite Materials*, Edinburgh, UK, Jul. 27–31.
- [21] De Marqui, C., Jr., Erturk, A., and Inman, D. J., 2009, "An Electromechanical Finite Element Model for Piezoelectric Energy Harvester Plates," *J. Sound Vib.*, **327**, pp. 9–25.
- [22] Albano, E., and Rodden, W. P., 1969, "A Doublet-Lattice Method for Calculating Lift Distributions on Oscillating Surfaces in Subsonic Flow," *AIAA J.*, **7**, pp. 279–285.
- [23] Dowell, E. H., Curtiss, H. C., Jr., Scalani, R. H., and Sisto, F., 1978, *A Modern Course in Aeroelasticity*, Sijthoff and Noordhoff, Alphen aan den Rijn, The Netherlands.
- [24] Hagood, N. W., and von Flotow, A., 1991, "Damping of Structural Vibrations

- With Piezoelectric Materials and Passive Electrical Networks,” *J. Sound Vib.*, **146**, pp. 243–268.
- [25] Renno, J. M., Daqaq, M. F., and Inman, D. J., 2009, “On the Optimal Energy Harvesting From a Vibration Source,” *J. Sound Vib.*, **320**(1–2), pp. 386–405.
- [26] Erturk, A., and Inman, D. J., 2009, “An Experimentally Validated Bimorph Cantilever Model for Piezoelectric Energy Harvesting From Base Excitations,” *Smart Mater. Struct.*, **18**, p. 025009.
- [27] Wang, Q.-M., and Cross, L. E., 1999, “Constitutive Equations of Symmetrical Triple Layer Piezoelectric Benders,” *IEEE Trans. Ultrason. Ferroelectr. Freq. Control*, **46**, pp. 1343–1351.
- [28] Harder, R. L., and Desmarais, R. N., 1972, “Interpolation Using Surface Splines,” *J. Aircr.*, **9**, pp. 189–191.
- [29] Hassig, H. J., 1971, “An Approximate True Damping Solution of the Flutter Equation by Determinant Iteration,” *J. Aircr.*, **8**(11), pp. 885–889.
- [30] Erturk, A., and Inman, D. J., 2008, “Issues in Mathematical Modeling of Piezoelectric Energy Harvesters,” *Smart Mater. Struct.*, **17**, p. 065016.
- [31] http://www.efunda.com/materials/piezo/material_data, accessed December 2008.
- [32] Erturk, A., Tarazaga, P. A., Farmer, J. R., and Inman, D. J., 2009, “Effect of Strain Nodes and Electrode Configuration on Piezoelectric Energy Harvesting From Cantilevered Beams,” *ASME J. Vib. Acoust.*, **131**, p. 011010.
- [33] Edberg, D. L., Bicos, A. S., Fuller, C. M., and Tracy, J. J., 1992, “Theoretical and Experimental Studies of a Truss Incorporating Active Members,” *J. Intell. Mater. Syst. Struct.*, **3**, pp. 333–347.
- [34] Fleming, A. J., Berhens, S., and Moheimani, S. O. R., 2000, “Synthetic Impedance for Implementation of Piezoelectric Shunt-Damping Circuits,” *Electron. Lett.*, **36**, pp. 1525–1526.